

Synthesis and functional verification of the unsupported active phase of V_xO_y catalysts for partial oxidation of *n*-butane

M. Hävecker^{a,*}, N. Pinna^b, K. Weiß^a, H. Sack-Kongehl^a, R.E. Jentoft^a, D. Wang^a, M. Swoboda^a, U. Wild^a, M. Niederberger^c, J. Urban^a, D.S. Su^a, R. Schlögl^a

^a Fritz-Haber-Institut der MPG, Dep. Inorganic Chemistry, Faradayweg 4-6, 14195 Berlin, Germany

^b Martin-Luther-Universität Halle-Wittenberg, Fachbereich Chemie, Institut für Anorganische Chemie, 06099 Halle (Saale), Germany

^c Max-Planck-Institute of Colloids and Interfaces, Colloid Dep. 14424 Potsdam, Germany

Received 2 August 2005; revised 29 September 2005; accepted 4 October 2005

Available online 4 November 2005

Abstract

We studied unsupported V_xO_y nanoparticles prepared by a novel nonaqueous route in the selective oxidation of *n*-butane to maleic anhydride. The evolution of the electronic and geometric structure of the material was characterized by X-ray photoemission spectroscopy, electron energy-loss spectroscopy, transmission electron microscopy, and electron diffraction before and after the reaction at different temperatures. A change from a water-mediated C–C bond cracking functionality of the catalyst forming acetic acid to an oxidizing functionality resulting in maleic anhydride was observed. It was found that the particles underwent a radical modification of the geometric and electronic structure that finally resulted in V_2O_5 crystals. Experimentally derived conclusions are related to some conceptual claims from the literature.

© 2005 Elsevier Inc. All rights reserved.

Keywords: Nanostructure; Vanadium oxide cluster; Microreactor; *n*-Butane oxidation; Structure/activity relationship

1. Introduction

Despite extensive research and contributions to the literature, the understanding of the mode of operation of vanadium-based oxidation catalysts remains incomplete [1–4, and references therein]. The technical catalyst for the oxidation of *n*-butane to maleic anhydride is vanadium-phosphorus-oxide (VPO) [5,6], a complex material composed of various phases [7–9]. Some experimental results suggest that in VPO, the structure of the catalytically active species is only weakly related to the average bulk structure [10,11]. It has been suggested that the VPO bulk acts as a support material and reservoir for the constituents of the active structure. Therefore, approaches to establish a structure–activity relationship for VPO based on bulk structural data would be at least ambiguous. It seems necessary to study model systems with a simplified structure but relevant catalytic properties.

In contrast to numerous studies of the structure–activity relationship of supported vanadium oxide catalysts [3,12, and references therein], here we investigated unsupported nanocrystals avoiding the complication of support effects. For catalysts containing an approximately monolayer coverage of surface vanadia, the number of converted *n*-butane molecules per vanadium atom was a strong function of the specific oxide support [13]. In our case, the V_xO_y nanoparticles were synthesized in a controlled manner via a simple nonaqueous process involving the reaction of vanadium isopropoxide with benzyl alcohol and subsequent solvothermal treatment [14]. This synthesis approach is widely applicable for the preparation of diverse metal oxide nanopowders with high purity, such as $BaTiO_3$ [15,16], SnO_2 , In_2O_3 [17], or HfO_2 [18]. A very small amount of the obtained vanadium oxide powder with a homogeneous, well-defined structure and defined morphology has been tested in a microreactor to study the catalytic properties.

This approach to investigating the catalytic function of a single-phase vanadium oxide has been taken previously and has concentrated on V_2O_5 [19,20]. It was found that sizeable ac-

* Corresponding author. Fax: +49 30 8413 4677.

E-mail address: mh@fhi-berlin.mpg.de (M. Hävecker).

tivity was always related to “reduced surfaces,” meaning that despite the claimed use of the phase V_2O_5 , the active material must have been of another structure. These pioneering studies were, in contrast to their intention, not carried out with model systems being discriminated from “real” catalysts by their rigorous geometric and electronic structural definitions. Thin V_2O_5 films of single crystal quality have recently become available [21–23]. Their reactivity even toward chemisorption was found to be negligible as long as their surface was long-range-ordered. Significant reactivity was detected after partial reduction by ion bombardment or by hydrogen atoms. The same observations hold for V_xO_y clusters deposited on single crystalline oxide supports.

Taking these observations into consideration, the hypothesis is put forward that catalytic activity depends on defects in V_xO_y phases. It should then be possible to minimize the energy necessary to create the beneficial defects containing the active sites for catalysis by fabricating nanostructured V_xO_y materials. A lower kinetic hindrance for restructuring into the active, defective form from the long-range order of the matrix phase can be expected for nanostructures exposing a sizable fraction of their constituting atoms as surface species and occurring in metastable morphologies and structural variants.

To fulfill the requirements of a model system, it is essential that a suitable structural definition of such a nanoparticle phase be achieved while its catalytic function is verified. Because defects are so relevant, conventional structural analysis with X-ray diffraction cannot be expected to be adequate. The present approach uses transmission electron microscopy (TEM) methodology as an analytical tool for geometric and electronic structure determination. This is adequate for nanostructured and defective materials, but requires great care when extrapolating from the local scale of the TEM observation to the integral scale of a catalyst test. Meaningful structure–activity relations can be

expected only if the scales of the experiments are brought together as closely as is experimentally possible. Such an attempt, focusing on the real structure or nanostructure of a functional model oxide, is made here. This was made possible by the construction of adequate equipment for both the reactor and the detector used in the catalytic testing. The key idea is to minimize the amount of catalyst used in testing, to approach a situation in which TEM data are representative for the whole catalyst. We used only an amount of material that fit on a standard TEM specimen grid for catalytic testing.

2. Experimental

2.1. Preparation

V_xO_y nanocrystals were synthesized by an alkoxide/benzyl alcohol route [14]. All of the synthesis procedures were carried out in a glovebox. Typically, 200 mg of the metal alkoxide vanadium(V) triisopropoxide was added to 20 ml of benzyl alcohol. The reaction mixture was transferred into a Teflon cup of 45 ml inner volume, slid into a steel autoclave, and sealed carefully. The autoclave was taken out of the glovebox and heated in a furnace (200 °C for 4 days). The resulting black suspension was centrifuged, and the precipitate was thoroughly washed with ethanol and dichloro methane and subsequently dried in air at 60 °C.

2.2. Catalytic tests

A reactor similar to that described in detail previously [24] was used for the catalytic tests of the material. A schematic drawing of the main components is shown as Fig. 1a. In brief, the sample was mounted onto a sapphire sample holder heated from the back by a NIR laser. The reactor has a volume of about

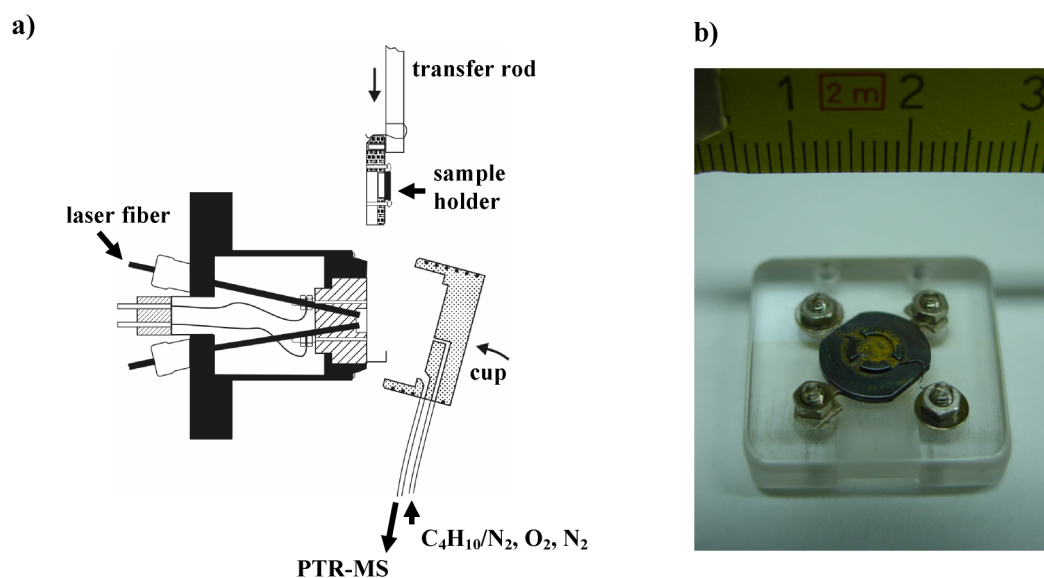


Fig. 1. (a) Schematic drawing of the reactor. Shown are the main components of the set-up: sample mounted on the sapphire, transfer rod to insert the sapphire into the reactor, movable cup to close the reactor, laser heating from the back. The gas feed is done via mass flow controllers. The reactor outlet is fed into the PTR-MS. (b) Sample holder used for the experiments. The sample suspension is deposited in the middle of the stainless steel support. This support is mounted onto a sapphire sample holder that is placed inside the reactor after the suspension dried.

4 ml. It can be opened using a moveable cup, and the sample can be transferred out of the reactor with no contact with ambient conditions.

For catalytic tests, the V_xO_y nanocrystals were first dispersed in ethanol, and then one drop of the suspension was released into a ring at the centre of a stainless steel support and dried in air. The ring has an inner diameter equal to the size of a typical TEM grid (around 2 mm). A thermocouple was spot-welded onto this ring for accurate temperature measurement. The stainless steel support was mounted onto a single crystal sapphire sample holder, as shown in Fig. 1b. Only a very small amount of catalyst was introduced into the reactor by this method; thus the entire amount of catalyst was exposed to identical conditions during the catalytic reaction.

The catalytic characterization was carried out under industrially relevant conditions (i.e., oxygen-rich conditions) at atmospheric pressure. High purity gases were used (butene < 1 vpm; butadiene < 0.1 vpm in *n*-butane). A mixture of *n*-butane (1 vol%), oxygen (16 vol%), and nitrogen (83 vol%) was fed into the reactor through calibrated mass flow controllers at a total flow rate of 22 sccm. The effluent reactor stream was fed in equal shares (11 sccm each) via heated capillaries into a differentially pumped electron impact mass spectrometer (PRISMA QMS 200; Pfeiffer) and into a proton transfer reactor–mass spectrometer (PTR-MS) (Ionicon Analytic).

The sensitivity of the electron impact mass spectrometer is approximately 10^{-14} mbar for small molecules like CO_2 , as stated by the manufacturer and confirmed by our own experience. Because of the differential pumping, this value corresponds to a minimum traceable concentration of 7–1 ppm of CO_x in the reactor.

A calibrated version of the PTR-MS (Ionicon Analytic) equipped with a heated gas inlet capillary system was used. The instrument was operated at a drift tube pressure of 2 mbar. The sample gas was continuously introduced into the chemical ionization cell. Only volatiles with proton affinities greater than water (proton affinity of H_2O , 166.5 kcal/mol) are ionized by proton transfer from H_3O^+ and subsequently mass-analyzed in a quadrupole mass spectrometer. Sensitivity for oxygenated molecules down to the sub-ppb level can be achieved.

The development of selected mass intensities was followed over time (multiple ion detection). The single dwell time for the different masses was adjusted to the concentration. Typically, the accumulation time per point was set to 5 s for maleic anhydride (MA) and to 2 s for all other expected species, including acetic acid, crotonaldehyde, 2,5-dihydrofuran, and furan. This resulted in an overall time resolution of approximately 4 data points/min if all masses of interest were recorded. Because of the soft energetics of ionization by proton transfer, mainly nondissociative reactions occur; that is, cracking of the target molecule is strongly inhibited. Therefore, nearly all intensity is expected to be recorded on the parent ion (molecule mass + 1 proton). Consequently, no ionization-induced fragmentation obscures the link between measured mass spectra and the actual gas composition, unlike in conventional electron impact mass spectrometry.

As outlined previously [25,26], a simple relationship exists between the experimentally measured PTR-MS intensities (in cps) and the actual absolute concentration in the gas stream. The transmission function of the quadrupole mass filter was taken into account. The temperature of the inlet system and the drift tube was 80 °C. A rate constant for the proton transfer reaction of $2 \times 10^{-9}/(cm^3 s)$ and a residence time of the reactants in the drift tube of 105 μs as given by the manufacturer was assumed.

Although a rather pure primary ion stream of H_3O^+ ions is delivered from the source, we checked for the formation of $(H_2O \cdot H_3O)^+$ clusters ($m = 37$ amu). Cluster formation may become important at high levels of humidity in the inlet gas stream. The formation of these clusters changes the reaction conditions in the drift tube, leading to an incorrect concentration determination. The proportion of these clusters remained well below 5% of the H_3O^+ ions under all conditions; thus, this process was neglected.

2.3. X-Ray photoelectron spectroscopy

Details of the electron spectrometer setup have been reported earlier [27]. A Leybold LHS 12 MCD instrument was used. The X-ray photoelectron spectroscopy (XPS) measurements were carried out in the pass energy mode (pass energy = 48 eV). The binding energy was calibrated to the $Au4f$ (84.0 eV) and $Cu2p_{3/2}$ (932.7 eV) core levels.

2.4. Transmission electron microscopy/electron energy-loss spectra

For initial transmission electron microscopy (TEM) investigations, the catalyst powder was removed from the sample holder with a spatula and placed onto a copper grid covered with a holey carbon film. A new sample holder transfer system in which the specimen transfer occurs without exposure to air in a glovebox is currently being implemented. All measurements were done with a Philips CM200 field-emission transmission electron microscope equipped with a Gatan energy filter GIF100 for electron energy-loss spectra (EELS) measurements. The microscope was operated at 200 kV. Electron diffraction patterns were evaluated before the corresponding EEL spectra were recorded.

2.5. Thermogravimetry and differential scanning calorimetry–mass spectrometry

Thermal analysis, using combined thermogravimetry (TG) and differential scanning calorimetry (DSC), was performed with a Netzsch STA 449C Jupiter instrument. Gas-phase products were transferred through a heated silica capillary from the TG/DSC to a Pfeiffer GSD 300 ThermoStar mass spectrometer running in multiple ion detection (MID) mode. The sample was heated in 21% oxygen in helium (100 ml/min) at a rate of 5 K/min up to 773 K. The sample was eventually held at 773 K for more than 10 h before it stopped gaining weight. MS was calibrated for CO_2 using a 0.5-ml pulse of pure CO_2 introduced

into the TG in a flow of He at a rate of 3 ml/min. MS was calibrated for water by heating $\text{Cu}(\text{SO}_4) \cdot 5\text{H}_2\text{O}$ in 100 ml/min of 21% oxygen in He at a rate of 5 K/min to 773 K. The last water peak at 450–550 K, equaling 1 mol water/mol Cu sulfate, was used.

3. Results

3.1. Catalytic activity

In one type of experiment (Fig. 2a), nanoparticles were heated sequentially from room temperature to 473, 573, and 673 K and then cooled to 323 K. The absolute amount of products can be compared in this experiment, because the same particles were used without removing material from the reactor. Afterward, the reaction was studied in more detail at different temperatures (473, 573, and 673 K) in single experiments (Figs. 2b–2d). The material remaining after these treatments was used for the XPS, EELS, and TEM studies, the results of which are presented in Figs. 4–7. A new drop of the particle/ethanol suspension was used for each temperature step. In these experiments, only the relative amount of products can be compared, because it cannot be ensured that exactly the same amount of material was placed in the active (i.e., hot) part of the sample holder in each experiment. The sequential heating experiment shown in Fig. 2a reveal that the onset of the selec-

tive *n*-butane oxidation to MA occurred already at temperatures as low as 473 K. Further heating to 573 K caused a strong increase in the MA signal (by a factor of 10). The MA signal remained almost constant with a further temperature increase to 673 K. The onset of the reaction at a relatively low temperature and the weakly increased MA with a temperature increase from 573 to 673 K is in marked contrast to the behavior of vanadium phosphorus-based catalysts, the materials used industrially for the selective oxidation of *n*-butane to MA. These catalysts show no activity at 473 K, but a strong increase in activity when the reaction temperature increases from 573 to 673 K.

The development over time was followed for several masses in detailed scans. Figs. 2b–2d show the traces for the masses 61, 71, and 99 amu (corresponding to molecule masses 60, 70, and 98 amu) at reaction temperatures of 473, 573, and 673 K, respectively. The signal on 99 amu can unambiguously be assigned to MA. It seems reasonable to relate the signal on 61 amu to acetic acid; the 71 amu intensity may be related to crotonaldehyde or dihydrofuran. Crotonaldehyde has been characterized as a byproduct of selective C_4 olefin oxidation [28]. It was not possible to distinguish isomers with the PTR-MS, because the identification of isomers by different fragmentation pattern (as in conventional electron impact MS) is not possible. Furthermore, traces of furan (molecule mass, 68 amu) could be detected at 673 K (not shown).

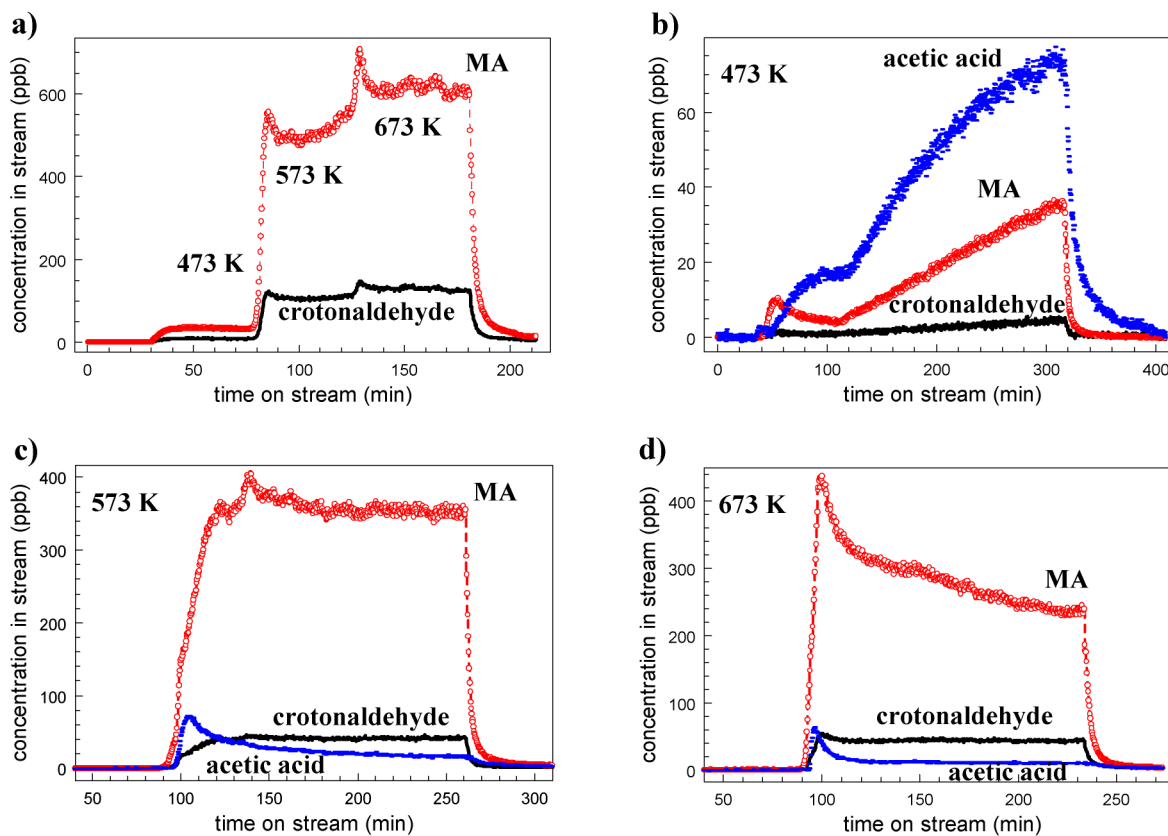


Fig. 2. PTR-MS response during the selective oxidation of *n*-butane. (a) Reaction profile of maleic anhydride (MA) and crotonaldehyde during sequential heating of VO_x nanoparticles to 473, 573, and 673 K, respectively, without taking the material out of the reactor. (b)–(d) Concentration of MA, crotonaldehyde and acetic acid when V_xO_y was heated to 473, 573, and 673 K, respectively. After each temperature step (b)–(d) the sample was taken out of the reactor and further characterized as described in the text. A new sample was prepared for each experiment.

Table 1

Concentration of acetic acid (61 amu protonated mass), crotonaldehyde (71 amu) and maleic anhydride (99 amu) derived from data presented in Fig. 2b–2d

Temperature	Concentration (ppb)		
	61 amu	71 amu	99 amu
200 °C	73.2	4.7	35.6
300 °C	17.6	41.6	354.1
400 °C	10.7	43.9	236.5

As mentioned earlier, the combustion products CO_x and the feed gases C_4H_{10} and O_2 could not be detected by PTR-MS, because these molecules are not protonated by H_3O^+ ions. CO_x also could not be detected by conventional electron impact MS during our experiment, presumably because of low concentration in the product stream. This fact limits the maximum amount of CO_x possibly present during the reaction to 7–1 ppm, taking the sensitivity of the electron impact MS into consideration (cf. Section 2.2). This estimation results in a selectivity to oxygenated products of 10–40%. These values compare reasonably well to the selectivities observed for model-supported vanadium oxide catalysts [13]. No conversion of C_4H_{10} and O_2 was detectable by conventional MS, setting the level of reaction to below 1%, which is reasonable when taking into account that only a few micrograms of catalyst were used. The test can be characterized as ideally differential. Thus, we used the productivity to the oxygenated products acetic acid, crotonaldehyde, and MA, with oxygenate selectivity defined as the product concentration (c_i) ratio

$$S_{\text{oxy},i} = \frac{c_i}{\sum_i c_i},$$

to get information on the structure–activity relationship for the material.

Fig. 2 shows that the relative abundances of these products varied significantly in the different temperature regimes. Their quantities are compiled in Table 1. The selectivity S_{oxy} of acetic acid, crotonaldehyde, and MA are shown in Fig. 3. Acetic acid was the dominating species in the gas phase at 473 K (Fig. 2b), with $S_{\text{oxy}} = 65\%$ (Fig. 3). The signal for this species and for MA increased with time on stream even after 300 min. This is taken as an indication of incomplete activation of the pre-catalysts similar to that observed in VPO systems.

MA was the predominant product (354 ppb) when the catalyst material was heated to 573 K (Fig. 2c), with $S_{\text{oxy}} = 86\%$ (Fig. 3). The signal intensity remained fairly constant over a 120-min period, indicating the catalyst's structural stability. The concentrations of acetic acid (18 ppb, $S_{\text{oxy}} = 4\%$) and crotonaldehyde (42 ppb, $S_{\text{oxy}} = 10\%$) concentrations were much lower than the MA concentrations. The acetic acid signal showed a peak immediately after reaching the reaction temperature of 573 K, followed by a steady decrease in concentration. This is considered evidence of the desorption/diffusion of a limiting constituent for this reaction channel, such as OH groups being lost as structural water.

Heating from room temperature to 673 K caused a peak in the MA and acetic acid signals, followed by a decrease with

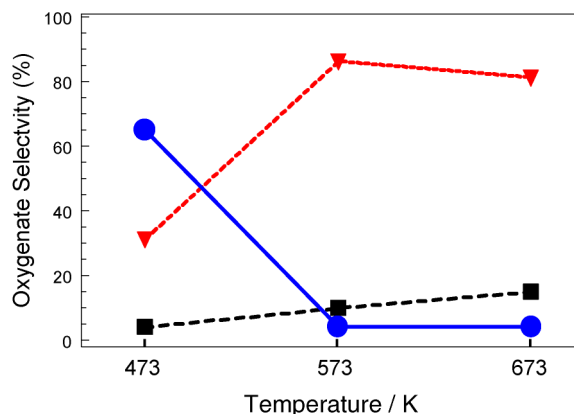


Fig. 3. Oxygenate selectivity S_{oxy} for MA (▼), acetic acid (●), and crotonaldehyde (■) at 473, 573, and 673 K derived from the data depicted in Fig. 2b–2d.

increasing time on stream (Fig. 2d). The MA concentration decreased from approximately 400 ppb at the beginning of the heating cycle to 220 ppb after 120 min. The acetic acid and crotonaldehyde concentrations were 11 ppb and 44 ppb, respectively. The corresponding selectivity, S_{oxy} , was 81% for MA, 4% for acetic acid, and 15% for crotonaldehyde (Fig. 3).

The reaction tests revealed a pronounced switching of the reactivity between a predominately C–C cleaving and oxidation mode at 473 K to a dehydrogenation and oxidation mode at 573 and 673 K. Two different catalysts were generated from a common precursor nanostructure by thermal activation in the feed. It should be possible to relate this change to structural differences of the final two catalysts. The data further show that the reactivity at 473 K is related to a slow process increasing the productivity. This points to a slow catalyst transformation and/or an insufficient reaction temperature and excludes the notion that the C–C cleaving process is achieved purely through gas-phase radical processes. Furthermore, the evolution of the oxygenate selectivity of crotonaldehyde (compared with that of MA) suggests a different parallel oxidative reaction pathway for this product.

3.2. The catalyst

3.2.1. Electronic structure

EELS probe the bulk electronic structure of individual, microscopically small particles. The shape of the vanadium L edges and the oxygen K edge is strongly related to the oxidation state of the vanadium and to the local geometric structure. As demonstrated in the literature [29,30], the intensity ratio of the V L_3 edge and the V L_2 edge (corresponding to electronic transitions $\text{V}2p_{3/2}-\text{V}3d$ and $\text{V}2p_{1/2}-\text{V}3d$, respectively) is related to the oxidation state of the absorber atom. The V L_2 edge is more intense than the V L_3 edge in V_2O_5 , whereas in a decreasing oxidation state, V L_2 intensity decreases relative to L_3 spectral weight [31]. The V L_3/L_2 ratios, given as the peak intensity ratios for reference compounds with a formal vanadium oxidation ranging from +2 to +5, are provided in Table 2. A clear trend becomes visible, with the exception of bulk V_2O_3 , which exhibits an unexpectedly high L_3/L_2 ratio. This anomaly of bulk V_2O_3 is probably due to other factors

Table 2
V L₃/L₂ EELS peak ratios for reference compounds with formal V oxidation states varying from +2 throughout +5 and of the catalyst after different thermal treatments in the gas feed

	Reference compounds					Catalyst			
	VO	V ₂ O ₃	V ₂ O ₄	V ₆ O ₁₃	V ₂ O ₅	293 K	473 K	573 K	673 K
Formal V oxidation state	+2	+3	+4	+4.3	+5				
V L ₃ /L ₂ peak ratio	1.12	1.21	1.02	0.99	0.96	1.08	1.05	1.00	0.98

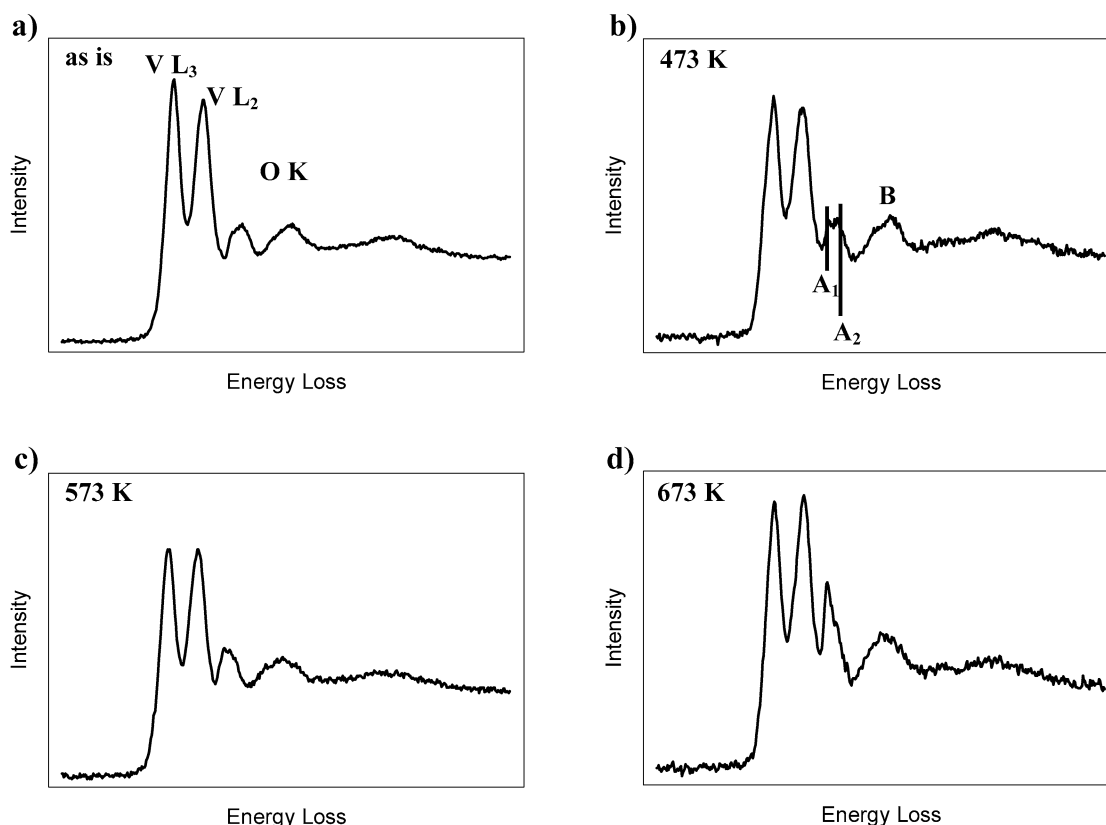


Fig. 4. EELS spectra of V_xO_y particles before (a) and after the reaction at 473 (b), 573 (c), and 673 K (d), respectively. The spectra can be divided into the V L edges at low energy loss followed by the O K edge at high energy loss as indicated.

(e.g., hybridization) than the V oxidation state that influences the *d*-state density and thus the white line peak ratio. Nevertheless, the V L₃/V L₂ edge intensity ratio is a fingerprint for assignment of the oxidation state. In the same manner, the intensity ratio of the resonances A1, A2, and B at the oxygen K edge are indicators of the oxidation state of binary vanadia species (cf. Fig. 4b). In general, resonance A1 gains intensity relative to A2 when the material becomes oxidized, and resonances A1 and A2 become more intense compared with resonance B.

Fig. 4 shows the EELS spectra of the as-synthesized material (a) and after prolonged treatment in the reaction mixture of *n*-butane and oxygen at 473, 573, and 673 K (b–d). The figure clearly shows a decreased V L₃/L₂ intensity ratio when the material was treated at higher temperatures. Although the V L₃ white line is more intense for the as-synthesized material and after heating in the reaction mixture to 473 K (Fig. 4a and 4b), the white line intensity is equal for the material heated to 573 K (Fig. 4c). Heating to 673 K resulted in a more intense V L₂

edge than V L₃ edge (Fig. 4d). The calculated V L₃/L₂ peak intensity ratio of the V_xO_y particles is summarized in Table 2.

Similar intensity variations can be seen at the oxygen K edge. The intensity of resonances A1 and A2 increased compared with resonance B during the treatment. Furthermore, the A1:A2 intensity ratio was modified by the treatment in *n*-butane and oxygen. Resonance A1 gained intensity during this process.

The surface electronic structure of the material was determined by XPS before the catalytic tests and after the treatment of the nanocrystals at 673 K in the reaction mixture. The macroscopic nature of standard XPS averages over the surface electronic structure of many nanoparticles and yields average information about the oxidation state. The XP vanadium 2*p*_{3/2} core level spectrum of the as-prepared material exhibited a broad, asymmetric line shape (Fig. 5a), indicating a variety of vanadium species of different valences. Taking the known binding energy of binary vanadium oxides into consideration, the as-prepared material consisted of vanadium species with a formal

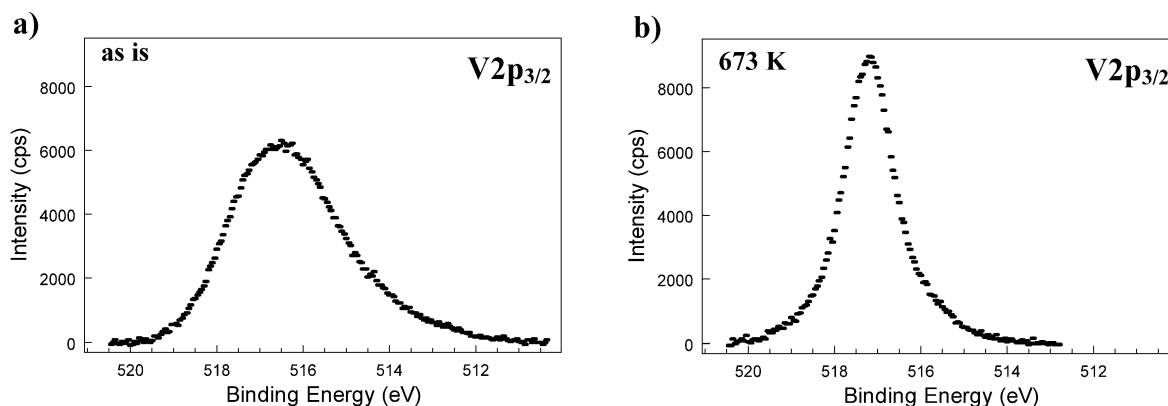


Fig. 5. $V2p_{3/2}$ core level XP spectra of the as synthesized V_xO_y nanoparticles (before the reaction) and of the material after the reaction at 673 K.

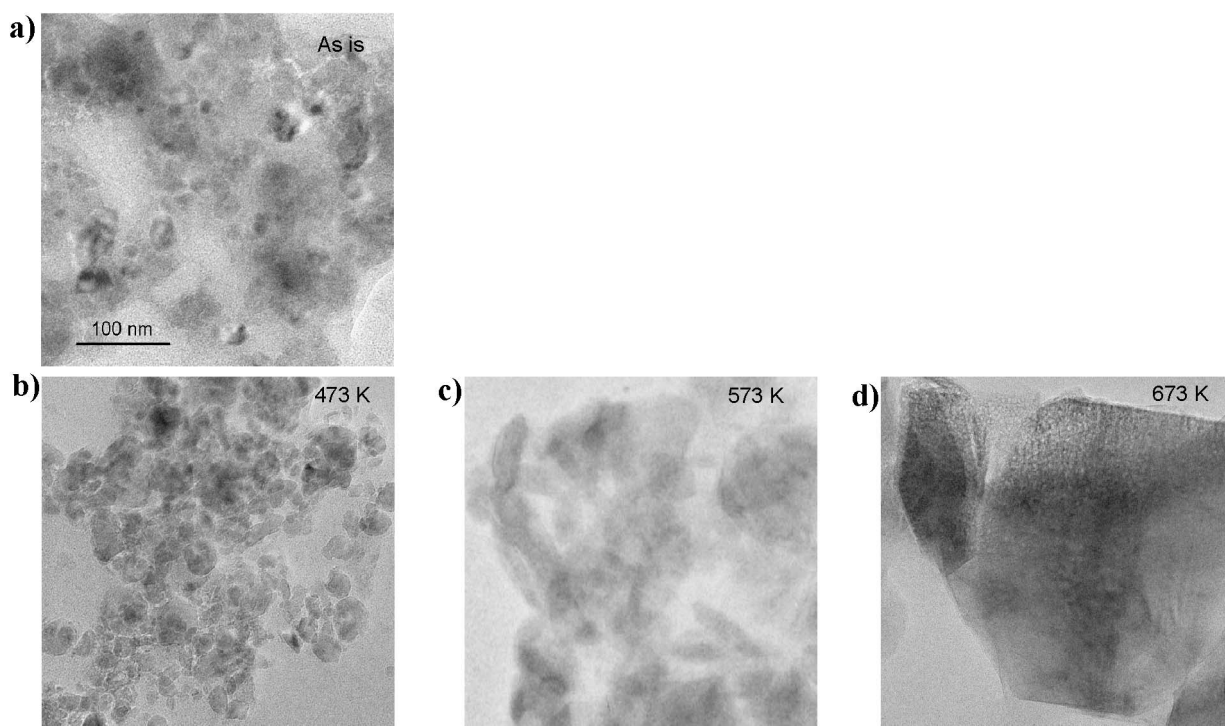


Fig. 6. TEM micrographs of the V_xO_y particles before (a) and after the reaction at 473 (b), 573 (c), and 673 K (d), respectively.

valence of +3 to +5. Details of the composition depend on the assumed line shapes, which are not known a priori. After the reaction at 673 K, the $V2p_{3/2}$ core level spectrum exhibits a sharp peak with a binding energy of 517.2 eV (Fig. 5b), consistent with this material's formal valence of +5.

Study of the electronic structure by XPS (averaging, surface-sensitive) and EELS (individual particle, bulk-sensitive) led to the conclusion that the as-synthesized material holds vanadium particles with varying oxidation states. Although mainly V^{3+} and V^{4+} were found by EELS, XPS demonstrated some amount of V^{5+} species at the surface as well. In the course of the reactions at different temperatures, the particles were oxidized by the feed gas. After prolonged treatment at 673 K, almost solely V^{5+} species were found by both EELS and XPS. The oxidation did not occur during sample transfer due to the reaction conditions, because almost no V^{5+} was found for the as-synthesized

particles. Thus, it was possible to tune the oxidation state of the nanoparticles by the thermal activation in the feed. A mixture of different vanadium oxidation states was always found in all but the final state after heating to 673 K.

3.2.2. Morphology and geometric structure

The oxidation process of the catalyst accompanied significant changes in morphology and geometric structure. Fig. 6 shows TEM micrographs of the material before (a) and after reaction at 473 (b), 573 (c), and 673 K (d), respectively. The material was converted to various small particles after reaction at 473 K, indicating the loss of structural water or other volatile species. Recrystallization started at 573 K. Finally, well-developed crystals resulted from the reaction at 673 K.

The structural dynamics of the material during the reaction was studied by electron diffraction. Fig. 7 shows characteristic

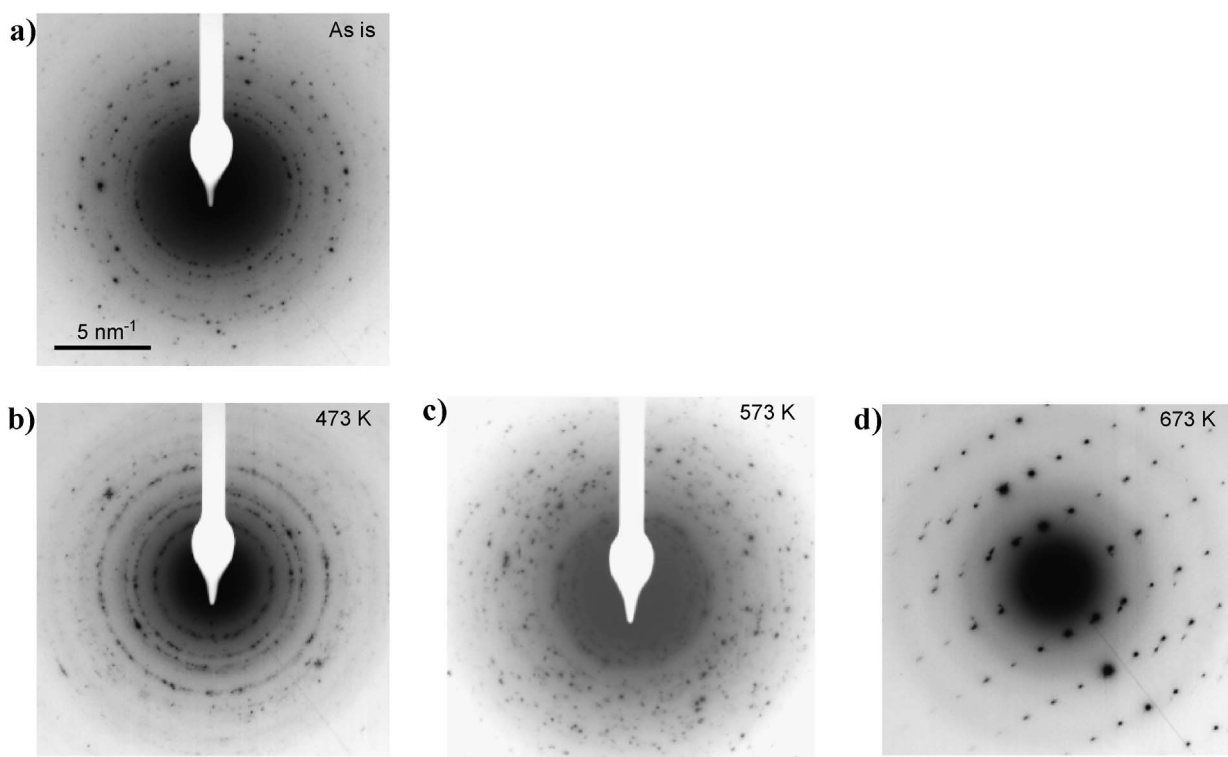


Fig. 7. Electron diffraction patterns of the V_xO_y particles before (a) and after the reaction at 473 (b), 573 (c), and 673 K (d), respectively.

Table 3

d -Spacings derived from the electron diffraction pattern of the material before the reaction. The value of 1.94 Å does neither belong to the structure of V_2O_4 nor V_2O_3

d Values measured (Å)	V_2O_4 (tetragonal)		V_2O_3 (rhombohedral)	
	d (Å)	(hkl)	d (Å)	(hkl)
2.69			2.71	(1 0 4)
2.44	2.42	(0 1 1)	2.48	(1 1 0)
2.16	2.14	(1 1 1)	2.19	(1 1 3)
1.94				
1.82			1.83	(0 2 4)
1.68	1.66	(1 2 1)	1.70	(1 1 6)
1.49			1.47	(2 1 4)
1.41			1.43	(3 0 0)

diffraction patterns of the material before (a) and after reaction at 473 (b), 573 (c), and 673 K (d). The diffraction patterns of the material before the reaction resulted in a mixture of mainly V_2O_3 and VO_2 crystallites, but other particles were also present, whose structure could not be identified as standard phases. Table 3 summarizes the analysis of the d -spacings of the material before the reaction. The main component of the material after the reaction at 473 K was VO_2 , although few crystallites were of an unidentified structure. No V_2O_3 nanocrystals were present after the treatment. After reaction at 573 K, no single vanadium oxide phase could be identified unambiguously from the electron diffraction pattern. The material seems to be a mixture of vanadium oxides, but the occurrence of VO_2 crystals can be excluded. Table 4 gives the measured d -spacings of the material after the treatment at 573 K and their assignments.

Table 4

d -Spacings derived from the electron diffraction pattern of the material after the reaction at 300 °C. Vanadium oxide phases with similar d -spacings are listed for comparison

d Values measured (Å)	V_2O_4 (unknown)	$VO_{1.27}$ (tetragonal)		V_3O_5 (monoclinic)		V_6O_{11} (triclinic)	
	d (Å)	d (Å)	(hkl)	d (Å)	(hkl)	d (Å)	(hkl)
3.38	3.31	3.37	(2 2 4)			3.31	(-1 2 0)
3.06		3.03	(5 1 2)			3.06	(-1 -1 7)
2.62	2.68	2.63	(6 0 2)	2.64	(-3 1 0)	2.62	(1 -2 4)
2.39	2.43	2.39	(4 4 4)	2.42	(-3 1 2)	2.42	(0 1 6)
2.02	2.03	2.06	(0 0 8)	2.00	(0 2 2)		
1.77				1.74	(-5 1 0)		
1.64	1.65			1.63	(-1 1 4)		
1.51				1.51	(-1 3 2)		

The material after the treatment at 673 K consists almost exclusively of V_2O_5 crystals, exposing their (0 0 1) surface to a large extent as basal plane.

3.2.3. Release of structural water

The reaction tests revealed a pronounced switching of the reactivity between a predominately C–C cleaving and oxidation mode at 473 K to a dehydrogenation and oxidation mode at 573 and 673 K. To elucidate the role of water release in this thermally activated process, the as-synthesized material was characterized using TG-DSC with gas-phase analysis by MS. Fig. 8 shows the results of this TG/DSC-MS measurement in 21% oxygen in He. The evolution of water ($m/z = 18$) and CO_2 ($m/z = 44$) was observed during particle heating. Water was removed from the sample with three maxima in concentration at

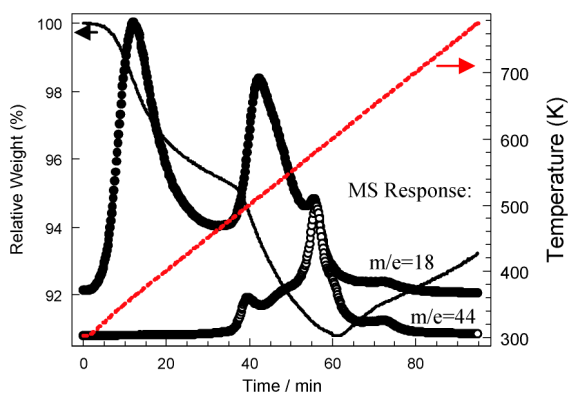


Fig. 8. Evolution of the relative weight during heating in 21% oxygen in helium, together with the MS signals for H₂O ($m/z = 18$) and CO₂ ($m/e = 44$).

363, 513, and 573 K. The first maximum in water was the desorption of physisorbed water with no other gas-phase products. The next, similarly broad, peak in the water concentration with a maximum at 513 K occurred simultaneously with an increase in CO₂ concentration, but the CO₂ evolution had a distinctly different profile (Fig. 8). Thus we conclude that most of the water production at 513 K resulted from a different process, that is, particle dehydroxylation. The final water peak at about 573 K was relatively sharp and had the same profile as the most rapid evolution of CO₂. Furthermore, this process coincided with an exothermal peak in the DSC signal (not shown), suggesting reactions at 573 K that produce both water and CO₂, presumably the combustion of residual CH_x groups from the preparation procedure.

The TG results show two weight loss steps ending at 483 and 613 K, followed by a weight increase. The first weight loss (about 5%) is ascribed to the desorption of water. Integration of the water signal and application of the calibration factor gave a value of 0.936 mg water lost during heating to 473 K. This finding is in good agreement with the weight loss of 0.90 mg measured by TG. In the second step, an additional 4.2% of the initial weight was lost. This weight loss is ascribed to the release of water and the combustion of hydrocarbon residuals, as mentioned earlier. Quantification of the gas-phase products allows an estimation of the mass loss due to these products. Based on the scenario that the hydrocarbon residuals have the general formula CH and that water evolving at temperatures above 473 K is from either hydrocarbon combustion or dehydroxylation, the gas-phase products equal 1.92 mg of adsorbed species. However, the weight loss from TG equaled only 1.77 mg. This difference is higher than the expected error for the gas-phase quantification (about 4%). Closing the mass balance requires another process, likely the further oxidation of the vanadium as suggested by the EELS data (Figs. 4b and 4c). Finally, the mass increased with increasing temperature after 613 K (about 2.4% of the initial weight) without further evolution of gas-phase products. This mass change is ascribed to the continued oxidation of the particles. After an extended period heating, this resulted in V₂O₅ (as seen on XRD). This final state can serve as a basis for calculating the vanadium valence at minimum sample mass, resulting in a vanadium valence of

4.5 at 613 K, consistent with the TEM, EELS, and XPS findings.

The TG-MS experiments allow us to attribute the change in the catalytic reactivity when the particles were heated from 473 to 573 K (Fig. 3) to the loss of OH groups as structural water.

4. Discussion

It is quite instructive to compare the catalytic behavior of the V_xO_y nanocrystals described in this report with the information about metal oxide-supported vanadia species found in the literature. In the case of supported vanadium oxide catalysts, it was reported that the turnover frequency in *n*-butane oxidation to MA declined above a loading exceeding monolayer coverage. It was concluded that this reflects the lower activity of microcrystalline V₂O₅ particles for the oxidation of butane; that is, microcrystalline vanadia was found to be detrimental to MA formation. The same mechanism seems to work in the case of unsupported V_xO_y nanocrystals as well.

Competitive reaction pathways are possible for an adsorbed organic intermediate. The selectivity pattern of the transformation of a specific intermediate depends on several factors, including the intrinsic activity of the active site to which the adspecies is adsorbed, the rates of surface migration or desorption of the adspecies, and the reactivity of the adspecies toward gaseous oxygen [32]. These factors are influenced by the specific surface characteristics. Oxygen availability plays a crucial role in reaction selectivity. In the presence of insufficient oxygen, partially oxidized species may desorb from the initial site at the surface of the catalyst. Consequently, the degree of reduction or the redox ability of the catalyst surface determines the reaction rate and selectivity to partial oxidation products.

A lower reaction temperature (compared with that for conventional VPO bulk catalyst for *n*-butane oxidation to MA) was also found in the case of supported vanadium oxide catalysts. Ruitenbeek et al. [33] and Wachs et al. [13] studied *n*-butane oxidation to MA on titania supported VPO catalysts and titania supported V₂O₅ catalyst, respectively. They found that selective oxidation occurred at a much lower temperature (493 K) than for conventional VPO catalysts. They concluded that the oxidation of butane to MA depends on both the redox properties and the acidic character of the bridging V–O support bond. Of course, this type of bond is missing for the unsupported V_xO_y nanocrystals studied in this report. Ruitenbeek et al. [33] concluded that the activity of titania-supported catalysts was related to their reducibility and to the average oxidation state of the vanadium ions on the surface.

The removal of moisture is thought to have a significant effect on catalytic activity. Surface vanadia species can become hydrated in the presence of moisture. Wachs et al. [12,13,34] reported significant moisture on metal oxide-supported vanadia species at temperatures below 473 K (several monolayers). Dehydration of the vanadia species seems to start above 473 K. Almost no moisture could be detected by Raman spectroscopy on these metal oxide-supported systems at 573 K. The strong activity increase and selectivity change observed in our exper-

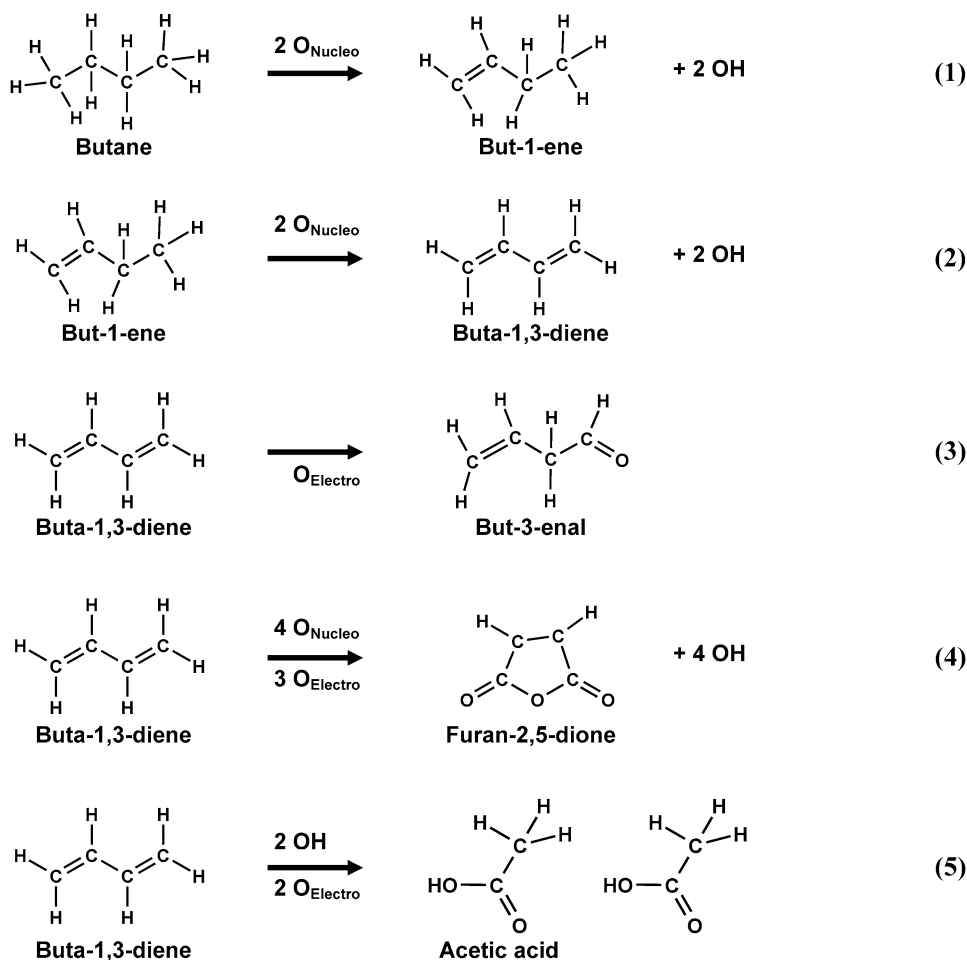


Fig. 9. Simplified reaction scheme of the selective oxidation of *n*-butane towards maleic anhydride.

iments when the catalyst was heated from 473 to 573 K coincided with the dehydroxylation of the nanoparticles as revealed by TG-MS.

The development of the catalytic activity during the isothermal experiments at 473 and 673 K (Figs. 2b and 2d) points to an evolution of the catalyst structure, whereas the steady-state behavior at 573 K seems to be the consequence of a mixture of phases. XPS and EELS studies revealed that the electronic structure of the nanoparticles changed from a variety of vanadium species with different oxidation states in the range of V^{3+} to V^{5+} to a material containing only V^{5+} species (Figs. 4 and 5). The formation of well-crystallized V_2O_5 is detrimental to the material's reactivity. This conclusion is supported by the fact that material that was heated to 673 K for a prolonged period had a lower MA yield when subsequently cooled to 473 K than material that was heated from room temperature to 473 K. Defective and nanostructured forms of bulk vanadium oxide seem to be the carrier of the catalytic activity that is absent in V_2O_5 (0 0 1) surfaces.

The analysis of the reaction as a function of temperature reveals two different reaction pathways, at 473 and 573 K. We suggest that two different catalyst species are responsible for this observation. Fig. 9 shows a simplified reaction scheme that explains the different functionalities of the catalyst material.

At high temperature, the catalyst exhibits both a dehydrating and an oxidizing functionality through nucleophilic oxygen, O_{Nucleo} , and electrophilic oxygen, O_{Electro} , respectively. This is demonstrated by the reactants O_{Nucleo} and O_{Electro} in Fig. 9. In addition, reactive protons (visualized as OH) existing at low temperatures may be created by the dehydrogenation products; at the very least, the O_{Electro} species must be bound to a reduced metal species. First, butane becomes two-fold dehydrogenated, resulting in an activated butadiene molecule (steps 1 and 2). At low temperatures, butadiene may be converted into activated ethylene through C–C bond cracking. Interestingly, ethylene has been observed as a byproduct for *n*-butane oxidation on VPO catalysts [35]. The ethylene molecules formally add water and become oxidized by aldehyde to acetic acid (step 5). This process may occur either as shown in Fig. 9 or sequentially. This C–C bond cracking functionality is missing at high temperatures; instead, the activated butadiene becomes oxidized, finally resulting in MA (step 4). In an additional, parallel pathway, the activated butadiene becomes oxidized to but-3-enal (step 3), finally resulting in crotonaldehyde (but-2-enal) through a rearrangement reaction.

From these assumptions about the reaction pathway, it can be concluded that at 473 K, the catalyst material must contain both V^{5+} sites that can be reduced (reversibly to V^{3+} or

V^{4+}) and active OH groups with C–C bond cracking functionality. Candidates for this kind of material are isopolycompounds, that is, complex hydrate-oxides. Typically, these compounds lose structural water at around 523 K and thus also lose the water-mediated C–C bond-cracking functionality, and subsequently the material forms oxides with complex structures. The TG-MS observation of water release with a maximum concentration at 513 K strongly supports this conclusion. At around 673 K, thermodynamic stable phases are formed due to the strong self-diffusion of oxygen in these compounds at this temperature. V_2O_5 or V_2O_4 may be formed, depending on the oxygen partial pressure. Consequently, the catalytic activity diminishes.

5. Conclusion

The data presented herein provide strong confirmation of the validity of the approach outlined in the Introduction. The application of chemical synthesis procedures from nanotechnology promotes access to reproducible precursors for fully functional model oxides of binary unsupported V_xO_y systems. In contrast to model-supported vanadium oxide catalysts, the unsupported model system provides direct access to structural data for the reactive material. It is possible to follow the material's structural transformation from a supramolecular system to the highly active selective oxidation phase and then to its deactivated stable form of V_2O_5 . The present study produced sufficient amounts of a single-phase active material. The amount of material used for catalytic testing was minimized, to approximate a situation in which the data obtained by TEM are representative of the whole catalyst. Morphological, geometric structural, and electronic structural details of the metastable state of V_xO_y were collected; these data can be used in developing experimentally supported structural models of the active sites. The transient character of the materials metastable under operation conditions and the strong influence of the operation conditions on formation and kinetic stability of the material has been highlighted.

The simultaneous detection of morphology, geometric structure, and electronic structure allows us to draw a series of conclusions about the nature of the active phase. These experimentally derived conclusions substantiate many conceptual claims from the extensive literature and allow us to draw a more consistent picture of the function of V_xO_y in partial oxidation. These conclusions are as follows:

- C–C bond cracking versus redox function. A selectivity change from acetic acid to MA was observed. This finding is ascribed to the change from the water-mediated C–C bond-cracking functionality forming acetic acid to the oxidizing functionality finally resulting in MA, as described in Fig. 9.
- Multiple sites. A steady formation of crotonaldehyde independent of the main reaction was found (Fig. 3), implying a parallel process.
- Relevance of the oxidation state. Pure V^{5+} is ineffective, but possibly only as it exists on defect-free surfaces

(vanadyl termination). The coexistence of V^{5+} and V^{4+} as an unavoidable consequence of structural defects is essential for selective oxidation function.

- Lattice oxygen. Defect formation is essential. Thus, deep lattice oxygen is an indicator for defect formation, not a source for selective oxygen (under operation conditions with gas-phase oxygen). Active sites require a minimum of two metal centres with flexible bridging where oxygen can be stored and activated. If one wishes to designate this dynamic defect formation and healing as “surface lattice oxygen,” then lattice oxygen is relevant. Then there arises the problem of distinction, because any normal catalyst also provides undercoordinated sites for activating and storing reactants. Thus the traditional statements that selective oxidation catalysts must have lattice oxygen and always follow kinetically the Mars–van Krevelan hypothesis are to be considered with reservation.
- Site isolation. The structural defects in V_xO_y provide site isolation both geometrically and electronically. It is current practice (although not essential) to achieve this by adding foreign atoms or promoters. In agreement with the literature, there seems to be good evidence that a dimer of vanadium with another metal (vanadium or other) is the core active site, highlighting the importance of reversible bridging of M–O–M substructures for selective oxidation.
- Design of good catalysts. The core property is the structural dynamics without allowing irreversible transformation in closely packed reduced forms. Open structures with a cluster-linker topology are most adequate, because they allow active sites isolated and stabilized by heteroatomic linkers into the matrix. The matrix may provide storage functions for active oxygen and electrons to buffer local deficits in chemical potential or preserve the topology of the active structure in temporal episodes of poor partial pressure of reactants.
- Phases. Neither well-developed and ordered phases of known binary oxides nor fully disordered or amorphous matrices are suitable for providing structural dynamics. Supramolecular units are strongly hydrated and provide extensive solid acid functions, leading to sometimes unwanted selectivity in C–C bond breaking. The successful system is a nanostructured extended solid.
- Supports. The nanostructure requires support to provide stability under the harsh reaction conditions. This can be provided by alumina silica or more functional supports, such as ceria or titania. The most suitable design seems to be self-supporting, however. The active oxide is self-supported very well on the bulk of the matrix or precursor structure. This minimizes the adverse effect of unwanted reactivity of the support surface (water-mediated C–C bond cracking) and optimizes the interaction of the active material with the support through homonuclear M–O–M bonds. For characterization of the active material, the problem of detecting an adlayer of similar composition but different structure arises.

Acknowledgments

Financial support was provided by SFB 546 of the Deutsche Forschungsgemeinschaft (DFG). The authors thank W. Ranke for providing the schematic drawing of the reactor.

References

- [1] E.A. Mamedov, V. Cortés Corberán, *Appl. Catal. A* 127 (1995) 1.
- [2] E. Hums, *Catal. Today* 42 (1998) 25.
- [3] B.M. Weckhuysen, D.E. Keller, *Catal. Today* 78 (2003) 25.
- [4] G. Centi (Ed.), Vanadyl Pyrophosphate Catalyst, in: *Catalysis Today*, vol. 16, Elsevier, Amsterdam, 1993, Part 1.
- [5] R.L. Bergmann, N.W. Frisch, US Patent 3,393,368 (1968), assigned to Princeton Chemical Research.
- [6] T.R. Felthouse, J.C. Burnett, S.F. Mitchell, M.J. Mummy, *Kirk–Othmer Encyclopedia of Chemical Technology*, Wiley, New York, 1995.
- [7] V.V. Gulians, J.B. Benzinger, N.Y. Sundaresan, I.E. Wachs, *Catal. Lett.* 32 (1995) 379.
- [8] G.J. Hutchings, J.A. Lopez-Sanchez, J.K. Bartley, J.M. Webster, A. Burrows, C.J. Kiely, A.F. Carley, C. Rhodes, M. Hävecker, A. Knop-Gericke, R.W. Meyer, R. Schlögl, J.C. Volta, M. Poliakoff, *J. Catal.* 208 (2002) 197.
- [9] I.E. Wachs, J.-M. Jehng, G. Deo, B.M. Weckhuysen, V.V. Gulians, J.B. Benzinger, *Catal. Today* 32 (1996) 47.
- [10] E. Kleimenov, H. Bluhm, M. Hävecker, A. Knop-Gericke, A. Pestyakov, D. Teschner, J.A. Lopez-Sanchez, J.K. Bartley, G.J. Hutchings, R. Schlögl, *Surface Sci.* 575 (2005) 181.
- [11] M. Hävecker, R.W. Mayer, A. Knop-Gericke, H. Bluhm, E. Kleimenov, A. Liskowski, D.S. Su, R. Follath, F.G. Requejo, D.F. Ogletree, M. Salmeron, J.A. Lopez-Sanchez, J.K. Bartley, G.J. Hutchings, R. Schlögl, *J. Phys. Chem. B* 107 (2003) 4587.
- [12] I.E. Wachs, B.M. Weckhuysen, *Appl. Catal. A* 157 (1997) 67.
- [13] I.E. Wachs, J.M. Jehng, G. Deo, B.M. Weckhuysen, V.V. Gulians, J.B. Benzinger, S. Sundaresan, *J. Catal.* 170 (1997) 75.
- [14] N. Pinna, M. Antonietti, M. Niederberger, *Colloids Surf. A* 250 (2004) 211.
- [15] M. Niederberger, N. Pinna, J. Polleux, M. Antonietti, *Angew. Chem. Int. Ed.* 43 (2004) 2270.
- [16] M. Niederberger, G. Garnweitner, N. Pinna, M. Antonietti, *J. Am. Chem. Soc.* 126 (2004) 9120.
- [17] N. Pinna, G. Neri, M. Antonietti, M. Niederberger, *Angew. Chem. Int. Ed.* 43 (2004) 4345.
- [18] N. Pinna, G. Garnweitner, M. Antonietti, M. Niederberger, *Adv. Mater.* 16 (2004) 2196.
- [19] J. Le Bars, J.C. Védrine, A. Auroux, B. Pommier, G.M. Pajonk, *J. Phys. Chem.* 96 (1992) 2217.
- [20] L. Owens, H.H. Kung, *J. Catal.* 144 (1993) 202.
- [21] A.-C. Dupuis, M. Abu Haija, B. Richter, H. Kühlenbeck, H.-J. Freund, *Surf. Sci.* 539 (2003) 99.
- [22] N. Magg, J.B. Giorgi, A. Hammoudeh, Th. Schroeder, M. Bäumer, H.-J. Freund, *J. Phys. Chem. B* 107 (2003) 9003.
- [23] N. Magg, J.B. Giorgi, M.M. Frank, B. Immaraporn, Th. Schroeder, M. Bäumer, H.-J. Freund, *J. Am. Chem. Soc.* 126 (2004) 3616.
- [24] C. Kuhrs, M. Swoboda, W. Weiss, *Top. Catal.* 15 (2001) 13.
- [25] W. Lindinger, A. Hansel, A. Jordan, *Int. J. Mass Spectrosc.* 173 (1998) 191.
- [26] W. Lindinger, A. Hansel, *Plasma Sources Sci. Technol.* 6 (1997) 111.
- [27] K. Noack, H. Zbinden, R. Schlögl, *Catal. Lett.* 4 (1990) 145.
- [28] G. Centi, F. Trifiro, J.R. Ebner, V.M. Franchetti, *Chem. Rev.* 88 (1988) 58.
- [29] R.D. Leapman, L.A. Grunes, *Phys. Rev. Lett.* 45 (1980) 397.
- [30] J. Fink, Th. Müller-Heinzerling, B. Scheerer, W. Speier, F.U. Hillebrecht, J.C. Fuggle, J. Zaanen, G.A. Sawatzky, *Phys. Rev. B* 32 (1985) 4899.
- [31] D.S. Su, M. Wieske, E. Beckmann, A. Blume, G. Mestl, R. Schlögl, *Catal. Lett.* 75 (2001) 81.
- [32] J.T. Gleaves, G. Centi, *Catal. Today* 16 (1993) 69.
- [33] M. Ruitenbeek, R.A. Overbeek, A.J. van Dillen, D.C. Koningsberger, J.W. Geus, *Recl. Trav. Chim. Pays-Bas* 115 (1996) 519.
- [34] I.E. Wachs, *Catal. Today* 27 (1996) 437.
- [35] B. Chen, E.J. Munson, *J. Am. Chem. Soc.* 124 (2002) 1638.